Research Article | Vol. 32, No. 14 / 1 Jul 2024 / Optics Express 24144
Optics EXPRESS

Advantages of internal reference in holographic shaping ps supercontinuum pulses through multimode optical fibers

LINDA PISCOPO,[1,2,6] LIAM COLLARD,[1,3] FILIPPO PISANO,[1,4] ANTONIO BALENA,[1,5] MASSIMO DE VITTORIO,[1,2,3,7] AND FERRUCCIO PISANELLO[1,3,8]

[1]*Istituto Italiano di Tecnologia, Center for Biomolecular Nanotechnologies, Arnesano, LE 73010, Italy*
[2]*Dipartimento di Ingegneria Dell'Innovazione, Università del Salento, Lecce 73100, Italy*
[3]*RAISE Ecosystem, Genova, Italy*
[4]*Department of Physics and Astronomy "G. Galilei", University of Padova, Via Marzolo 8, 35131, Padova, Italy*
[5]*Laboratoire Kastler Brossel, Sorbonne University, CNRS, ENS-PSL University, Collège de France, Paris, 75005, France*
[6]*linda.piscopo@iit.it*
[7]*massimo.devittorio@iit.it*
[8]*ferruccio.pisanello@iit.it*

Abstract: The use of wavefront shaping has found extensive application to develop ultra-thin endoscopic techniques based on multimode optical fibers (MMF), leveraging on the ability to control modal interference at the fiber's distal end. Although several techniques have been developed to achieve MMF-based laser-scanning imaging, the use of short laser pulses is still a challenging application. This is due to the intrinsic delay and temporal broadening introduced by the fiber itself, which requires additional compensation optics on the reference beam during the calibration procedure. Here we combine the use of a supercontinuum laser and an internal reference-based wavefront shaping system to produce focused spot scanning in multiple planes at the output of a step-index multimode fiber, without the requirement of a delay line or pulse pre-compensation. We benchmarked the performances of internal vs external reference during calibration, finding that the use of an internal reference grants better focusing efficiency. The system was characterized at different wavelengths, showcasing the wavelength resiliency of the different parameters. Lastly, the scanning of focal planes beyond the fiber facet was achieved by exploiting the chromato-axial memory effect.

1. Introduction

Neural tissue endoscopy has emerged as a promising tool for studying local microcircuitry [1] in deep brain regions, enabling cell type-specific mapping of neural activity [2], observation of sub-cellular structures [3], and investigation of related physiological and pathological states [4], in a minimally invasive fashion. Fiber bundles [5–7] and graded index (GRIN) lenses [8] are greatly supporting neuroscientists, facilitating imaging of sub-cortical structures. However, the demand for ultra-compact implant cross-sections has driven the advancement of endoscopic techniques based on multimode optical fibers (MMFs). MMFs can indeed carry a wealth of information with thousands of modes guided within a 50 μm diameter core [9]. Despite guided modes are mixed into a seemingly random speckle pattern at the output facet [10], the phenomenon is a deterministic process that can be controlled by employing optimization algorithms that leverage the estimate the fiber transmission matrix (TM) [11]. These methods include phase modulation techniques based on spatial light modulators (SLMs) or digital micromirror devices (DMDs) [12–14]: the

#528043 https://doi.org/10.1364/OE.528043
Journal © 2024 Received 25 Apr 2024; revised 31 May 2024; accepted 4 Jun 2024; published 17 Jun 2024

Optics EXPRESS

TM is assessed by iterative interferometric measures, detecting the interferogram between a varying-phase hologram propagated through the MMF [15] (the probe beam) and a fixed-phase reference that can be external or internal to the MMF. Interesting alternatives are represented by digital phase conjugation [16] and phase retrieval [17,18] algorithms with the advantage of not relying on interferometric measurement based on references but requiring complex alignments or leading to lower light confinement in the focused spots. Another reference-free class of techniques that have emerged over the years are based on machine learning algorithms [19–21]. These techniques may be advantageous due to their resilience to dynamic perturbation of the TM [22,23], such as bending and temperature but demand extensive amounts of data [24]. These paradigms pushed the performances of MMF endoscopy, harnessing the speckles to structure output light and obtain diffraction-limited raster-scanning imaging [25], super-resolution nanoscopy [26], and time of flight measurements for reconstructing three-dimensional images several centimeters beyond the fiber tip [27].

A frontier topic is represented by the translation to the realm of MMF endoscopy of a set of microscopic techniques requiring the use of visible or near-infrared light excitation short pulses including two-photon (2P) imaging [28,29], fluorescence lifetime imaging (FLIM) [30] and coherent anti-stokes Raman spectroscopy (CARS) [31,32]. These applications require broadband wavelength tunability to fully enable the operator to optimize the excitation for the employed fluorescent reporters (for instance for FLIM), or to better exploit non-linear phenomena (such as 2P absorption or CARS). Aside from the spectral requirements, the use of wavelength-tunable short pulses sources adds another level of complexity, since the short pulses of the light source (∼100 fs) guided into the MMF undergo temporal broadenings due to modal dispersion. This affects the interferometric measurements required to estimate the TM by reducing the probability of a temporal overlap across the output measurement plane. In fact, when the radiation is pulsed, the interference of the internal modes with the reference beam at the measurement plane can occur only if the internal modes of the fiber overlap in space and time with the reference pulse. This caveat can be addressed by adding an adjustable delay line on the external reference beam, to select only the modes with similar propagation velocities directly during the interferogram measurement [31,33]. Nevertheless, in addition to complicating the optical path, this method introduces a temporal overlap between the probe and reference pulses that remains only partial owing to their distinct temporal broadening, thereby diminishing the overall efficiency of the process. An alternative strategy lies in temporal focusing, necessitating the utilization of temporal wavefront shaping on a beam that has already undergone spatial shaping. However, this method demands extended computational time and additional optical components. [34].

Here we describe how the combination of an internal reference with a supercontinuum light source can be employed to obtain volumetric raster scanning of a picosecond-pulsed beam at multiple wavelengths generated by a photonic crystal fiber. The internal reference undergoes similar dispersion and delaying effects affecting the probe beam, avoiding the propagation-velocity filtering that instead characterizes systems based on a delayed external reference. This removes the need for an external adaptable delay line, streamlines the optical setup, and enhances focusing efficiency within the focused spot but does not allow control of the temporal profile of the pulse propagating inside the fiber. Tiny variations (1 nm) of the source wavelength enable the chromato-axial memory effect to move the raster-scanning plane along the fiber axis, while multi-wavelength calibrations warrant the use of the system in multiple spectral ranges.

2. Results

2.1. Operating principle and optical path

To properly shape the light intensity pattern at the output of a MMF, a preliminary calibration step [35] is required. The calibration procedure consists of measuring the interference patterns

Optics EXPRESS

$I^{ref}_{probe}(x^{in}_{i_1}, y^{in}_{i_2}, \phi_i)$ between several probe beams $B_{probe}(x^{in}_{i_1}, y^{in}_{i_2}, \phi_i)$ transmitted sequentially through the MMF and a reference beam $B_{ref}(x_{ref}, y_{ref})$, where $(x^{in}_{i_1}, y^{in}_{i_2})$ identifies different positions of the probe beam at the fiber input, hereafter referred to as "*external spatial modes*". $B_{ref}(x_{ref}, y_{ref})$ is instead injected at a fixed location (Fig. 1(A), "internal reference") at the input facet or skips the fiber to implement an "external reference" configuration, used for comparison (Fig. 1(B)). For each $(x^{in}_{i_1}, y^{in}_{i_2})$ input position, the phase of the probe beam ϕ_i is varied between 0 and 2π. Then, an optimization algorithm operates on the recorded $I^{ref}_{probe}(x^{in}_{i_1}, y^{in}_{i_2}, \phi_i)$ to identify the optimum ϕ_i value that generates constructive interference at a target output position at the distal fiber facet $\left(x^{out}_{j_1}, y_{j_2{}^{out}}\right)$ (see planes definitions in Fig. 1(A)). This allows identifying the phase wavefront that needs to be injected in the MMF input to obtain a diffraction-limited focused spot at the output of the MMF [36]. During the calibration procedure, each of the external spatial modes $(x^{in}_{i_1}, y^{in}_{i_2})$ is decomposed into the internal guided modes of the MMF. For pulsed coherent light, the interference of the internal modes with the reference beam at the output facet can occur only if the internal modes of the fiber overlap in space and time with the reference pulse. To compensate for this, methods using an external reference need an adjustable delay line that must be tuned to match the temporal delay arising from the propagation velocities of different modal subsets [37]. This, in turn, results in a more complex optical path, but also in a sub-optimal temporal overlap [33]. Indeed, the external reference and the probe beams undergo to different dispersions, resulting in a different pulse broadening and effective interference in a time window shorter than the broadened pulse of B_{probe} (Fig. 1(B)). The use of an internal reference would instead allow B_{probe} and B_{ref} to experience similar modal dispersion inside the MMF (Fig. 1(A)).

To test this hypothesis, we employed the optical setup depicted in Fig. 1(C), composed of three main sections: (i) a supercontinuum generation module, (ii) a wavelength selection block, and (iii) a phase modulation block. In the first block, a 785 nm fs-pulsed laser (TOPTICA FemtoFiber smart 780, pulse duration ~93 fs) is expanded by lenses L1 (focal length $f_{L1} = 75$ mm) and L2 ($f_{L2} = 300$ mm) and then focused by Obj1 (0.5 NA, 20x, RMS20x-PF, Olympus) on the facet of a 12 cm-long photonic crystal fiber (PCF, NKTPhotonics, FemtoWHITE 800), using a λ/2 waveplate to match the laser polarization with the principal polarization axis of the PCF. Due to the extreme confinement in the photonic crystal, the laser interacts non-linearly with the PCF core, broadening the laser spectrum. The pump laser wavelength was chosen to be larger than the zero-dispersion wavelength ($\lambda_{zero} = 750nm$) of the PCF to obtain a broader spectrum [38]. The supercontinuum beam generated by the PCF is collected by Obj2 (0.5 NA, 20x, RMS20x-PF, Olympus) and focused by an achromatic doublet L4 (AC-254-100-AB-ML, $f_{L4} = 100$ mm) on the input slits of a monochromator (HORIBA, microHR, $f/\#_{MC} = 3.88$). The achromatic doublet focal length was chosen to match the f-number of the monochromator ($f/\#_{L4} = 3.9$). The angularly dispersed output light, with a spectral dispersion on the slit plane of 5.25 nm/mm, was filtered with a slit and collimated with lens L5 ($f_{L5} = 35$ mm). The filtered light was then routed towards a phase-only spatial light modulator (SLM, ODP512, Meadowlark Optics), using a λ/2 waveplate to match the polarization of the collimated beam to the SLM modulation axis. After the waveplate, a beam expander, composed of the lenses L6 ($f_{L6} = 25$ mm) and L7 ($f_{L7} = 250$ mm), resized the beam to slightly overfill the SLM screen. The screen of the SLM was conjugated with the back focal plane of Obj3 (0.65 NA, 40x, AMEP4625, ThermoFisher) by a 4f system consisting of the lenses L8 ($f_{L8} = 400$ mm) and L9 ($f_{L9} = 200$ mm). Obj3 focused the modulated wavefront on the back facet of an MMF segment (0.22 NA, 50 μm core diameter, Thorlabs FG050UGA). The MMF employed in the experiments was 50 mm in length, compatible with endoscopic applications in mouse brain imaging [1,39]. While propagating through the fiber, both B_{probe} and B_{ref} supercontinuum pulses experience modal dispersion, due to the different propagation velocities of the internal modes, with the fiber length having an impact on the resulting average temporal broadening of the pulse. The temporal difference $\Delta\tau$ between the longer and the shortest

Optics EXPRESS

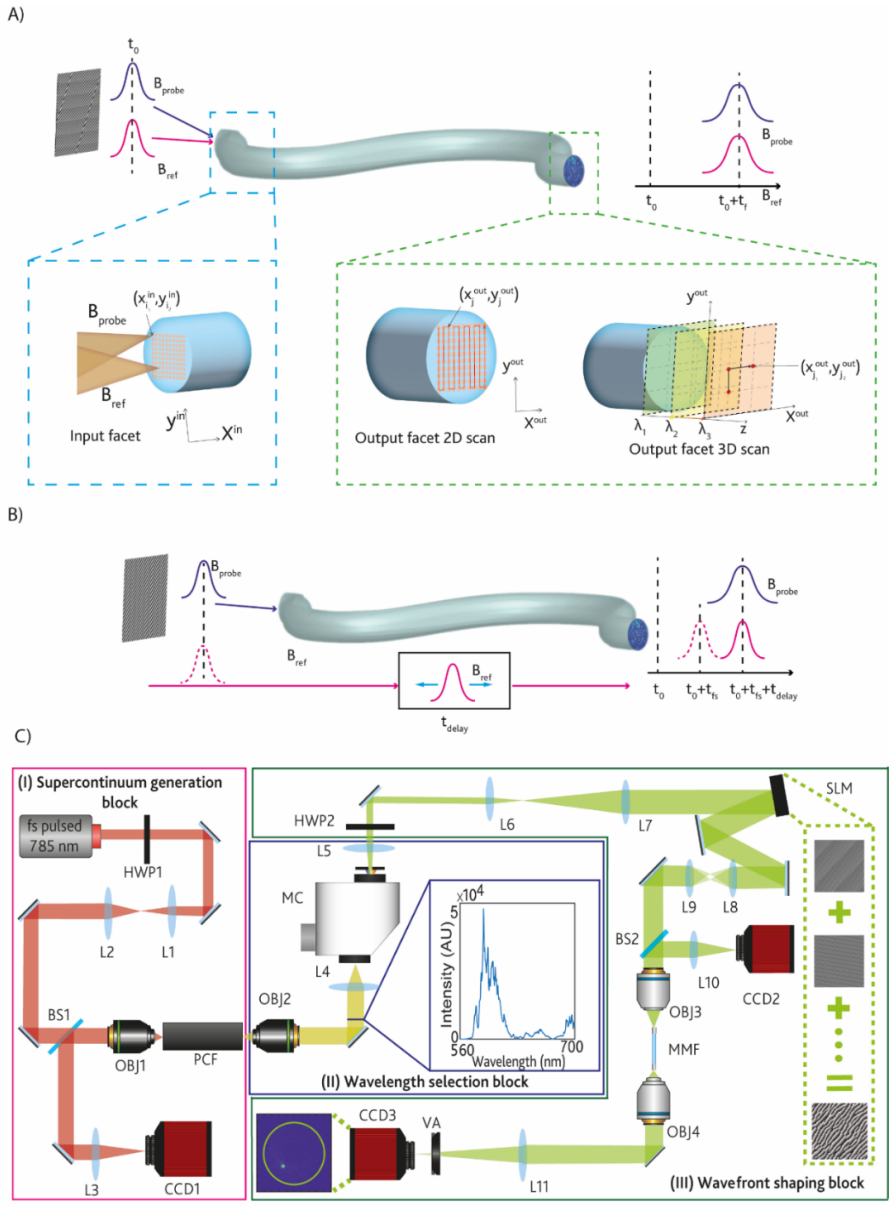

Fig. 1. Graphical representation of the working principle of the calibration algorithm for internal reference. The resultant scanning foci at the output of the multimode fiber are shown in the central panel. The possibility to tune the wavelengths allows moving the focused spot in the z-axes for a volumetric scan (right panel). B) Graphical representation of the working principle of the calibration algorithm for external reference based systems. C) Schematic representation of the optical setup, divided into three main blocks: (I) supercontinuum generation, (II) wavelength selection and (III) wavefront shaping. In (II) an example of supercontinuum spectrum in the visible range obtained with a polarization angle of 45° to the optical table and input coupled power of 46 mW is presented. Optical elements: HWP – half wave plate, L – lens, BS – beamsplitter, CCD –charged coupling device, OBJ –microscope objective, PCF- photonic crystal fiber, MC- monochromator, SLM - spatial light modulator, MMF – multimode fiber, VA –variable attenuator.

Optics EXPRESS

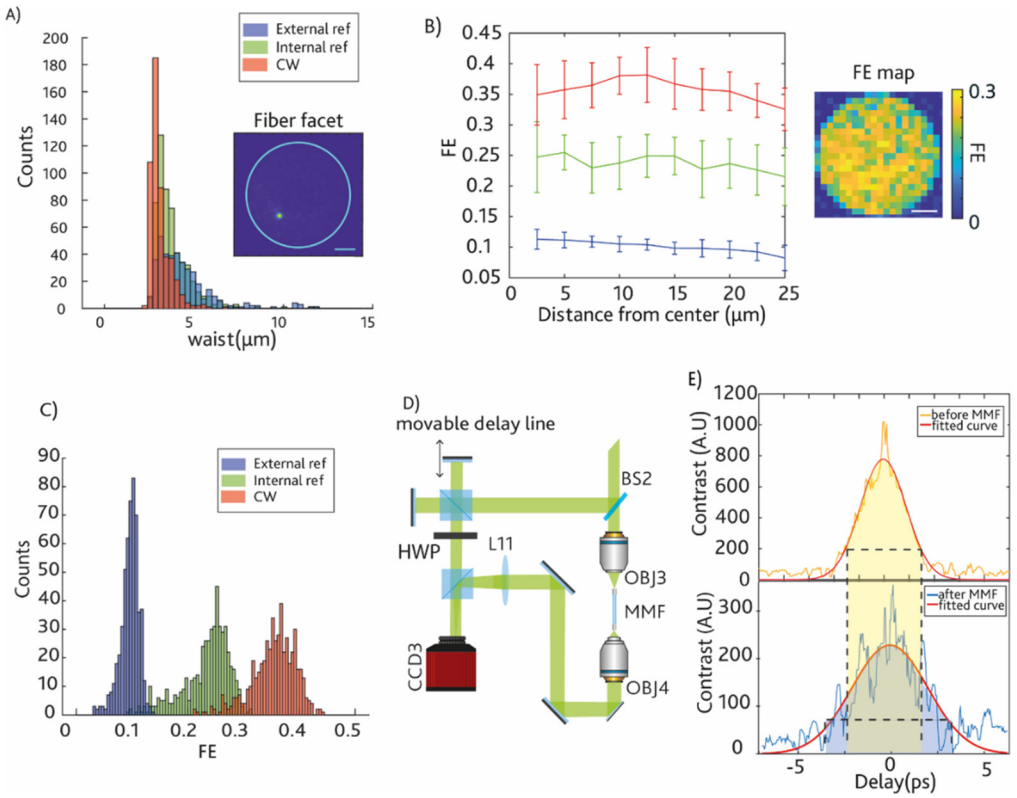

Fig. 2. A) Waist distribution of focused spot on the fiber output facet. The scale bar represents 10 μm. B) Left: radial distribution of the FE for internal reference CW laser emitting at 633 nm in red, in green internal reference using the SC pulsed laser at 600 nm and external reference in blue. Right: Focusing efficiency map obtained in internal reference configuration using SC pulsed laser. The scale bar represents 10 μm.C) FE distribution obtained with external reference and internal reference using a pulsed source. For comparison, FE distribution obtained with internal reference and CW laser source emitting at 633 nm is also presented. D) Optical setup closeup of external reference and autocorrelator path. E) Autocorrelation measures for the beam before the optical fiber and after. The measurement is carried out at 600 nm.

optical path that a mode can follow inside the core can be estimated as $\Delta\tau = \frac{NA^2 L}{c n_{core}}$, where NA is the numerical aperture of the fiber, L is its length, n_{core} is the core refractive index, and c is the speed of light in vacuum [27]. For the fibers used in this work NA = 0.22, $L = 50$ mm, $n_{core} = 1.458$, resulting in $\Delta\tau = 5.5$ ps. The speckle patterns at the fiber output were collected by Obj4 (0.65 NA, 40x, RMS40X, Olympus) and imaged on a charged coupled device (CCD) by L11 (f = 125 mm). To increase the confinement of light inside the focused spot, additional control over the polarization can be added. This will entail the splitting of the probing and reference beam into two [12], further complicating the optical path.

To generate the external spatial modes $B_{probe}(x_{i_1}^{in}, y_{i_2}^{in}, \phi_i)$, blazed phase gratings with different orientations were employed to define a 50×50 input matrix (Fig. 1(A), left), and for each four phase steps were tested $\left(\phi_i = 0, \frac{\pi}{2}, \pi, \frac{3\pi}{2}\right)$. The 2500 elements of the input matrix allow to generate a number of external spatial modes higher than the number of guided modes at each of the tested wavelengths ($M = \frac{1}{2}\left(\frac{2\pi r}{\lambda} NA\right)^2$), a condition warranting to exploit the full modulational

Optics EXPRESS

capabilities through MMFs. The reference beam $B_{ref}(x_{ref}, y_{ref})$ was generated by an additional grating and focused on the MMF on a fixed (x_{ref}, y_{ref}) position or directed toward a delay line for comparison. Before displaying on the SLM, the gratings were Fourier transformed and summed. For every $(x_{i_1}^{in},\ y_{i_2}^{in})$, the optimal phase shift ϕ_i^{opt} that gives the maximum intensity value for each pair of coordinates $(x_{j_1}^{out},\ y_{j_2}^{out})$ was stored (see Supplement 1). By summing the gratings generating $B_{probe}(x_{i_1}^{in}, y_{i_2}^{in}, \phi_i^{opt})$ in the Fourier plane, the optimized input phase modulation masks (green dashed box in Fig. 1(C)) are generated to scan the focused spots in each of $(x_{j_1}^{out},\ y_{j_2}^{out})$ of a 30 by 30 array on the output facet (Fig. 1(A), center).

In the following, the optical system and the described algorithm are fist employed to benchmark the differences between using a pulsed laser with an internal or external reference and versus the case of a continuum wave laser. Later, the resiliency to wavelength and the implementation of the chromato-axial memory effect to generate three-dimensional raster scanning grids are analysed.

2.2. Focusing short pulses with internal reference

A focused spot scanning across the output facet obtained with the above-described system tuned at λ = 600 nm is displayed in Visualization 1, with a representative frame reported in the inset of Fig. 2(A). A beam waist ($1/e^2$ of the maximum) estimation gave $w_{int} = 4.28 \pm 1.18\ \mu$m (mean ± standard deviation, n = 550) over the entire scanning field, approaching the diffraction limit related to the fiber NA ($\frac{1.22\lambda}{NA} = 3.32$ μm). The same characterization was performed with an external reference beam and produced a statistically indistinguishable average beam waist $w_{ext} = 4.53 \pm 1.70\ \mu m$ (p = 0.063, t-test, the delay line was optimized to give the highest fringes contrast in the interferometric calibration procedure). For comparison, a continuous wave (CW) laser at λ = 633 nm in internal reference configuration gave $w_{cw} = 3.13 \pm 0.70\ \mu m$. The statistical distribution of the obtained waists across the fiber core is reported by the histograms in Fig. 2(A).

For each $(x_{j_1}^{out},\ y_{j_2}^{out})$ on the output facet, the quality of the calibration process was estimated by calculating the focusing efficiency, defined as intensity in the focused spot divided by the intensity in the overall core of the fiber [13,15]:

$$FE(x^{out}, y^{out}) = \frac{\sum_{(j_1^2+j_2^2)<w^2} I(x_{j_1}^{out}, y_{j_2}^{out})}{\sum_{(j_1^2+j_2^2)<D^2} I(x_{j_1}^{out}, y_{j_2}^{out})} < 1,$$

where $D = 50\ \mu$m is the fiber diameter. A relatively uniform FE was obtained across the facet (insert in Fig. 2(B)), with a slight decrease as a function of the distance from the core (green line in Fig. 2(B)). Comparison with external reference data (blue line) shows a higher FE for the internal reference calibration, which is confirmed by the overall FE distribution reported in Fig. 2(C). In terms of average value, we obtained $FE_{int} = 0.22$ (standard deviation 0.04, n = 550) for the internal reference and $FE_{ext} = 0.096$ (std 0.004, n = 550) for delayed external reference, quantifying a ~ 2.3 times increase. This difference can be explained by considering the temporal characteristic of the pulse duration before and after the MMF, which was measured using an autocorrelation technique implemented with a Michelson interferometer (Fig. 2(D)). The pulse duration before the transmission through the fiber (which is also the pulse duration of the external reference) was estimated to be $\tau_{ref} \sim 1.67 \pm 0.10$ ps, while the pulsed speckle pattern duration after the transmission through the fiber was found to be $\tau_{probe} \sim 2.6 \pm 0.5$ ps. As a result, even if in the external reference scheme a delay line is employed to temporally synchronize the two pulses, the pulse transmitted through the MMF will be approximately 36% wider than the reference pulse (Fig. 2(E)) and the interference will happen only in the overlapping portion of the pulses (see overlapping area in Fig. 2(E)). This supports the hypothesis that an internal reference allows a better overlap of the probe and the reference pulses during calibration. Additionally, the use of an internal reference has the advantage of higher stability due to the common optical path between the probing beam and the reference, and low sensitivity to the alignment of the setup [9,27].

Optics EXPRESS

However, a certain degree of mismatch persists also in the case of the internal reference, due to the low interferometric compatibility of guided modes that experience low or extreme delays with the internal reference. As a result, CW implementations achieve better FE performances, as shown by the comparative data reported in red Fig. 2(B) and (C) ($\lambda_{CW} = 633$ nm, internal reference, $FE_{CW} = 0.34$, std 0.05, n = 550).

2.3. Wavelength resilience and chromato-axial volumetric scan

One of the major benefits of employing a pulsed supercontinuum source is the possibility of changing the operational wavelength of the scanning system while preserving coherence. We therefore investigated the properties of the system by calibrating it at either λ_i = 570, 600 and 633 nm, scanning the output facet of the MMF in 30 × 30 array. In all cases, an internal reference beam was used. The focusing efficiency map at the output facet reveals a similar trend for each employed λ_i, in terms of both FE spatial and intensity distribution (Fig. 3(A) and 3(B), respectively). Both the average FE and the FE variation as a function of the radial position remain consistent across the three wavelengths (Fig. 3(C) and 3(D), respectively). On average, across radii and wavelengths, ~22% of the light is coupled into the focused spot, showcasing the system's resilience across different wavelengths. Small variations of the average FE are likely due to a variability in the stability of the optical setup over the transmission matrix measurement (e.g. thermal expansion of optomechanical components).

For an increasing wavelength, the distribution behavior of the waist size is preserved (Fig. 3(E)), with the expected waist increase as dictated by the diffraction limit (Fig. 3(F)). This is accompanied also by a bigger size as the focused spot moves towards the edge of the fiber core (Fig. 3(G)), in agreement with other literature reports for CW lasers [40]. For the three wavelengths the pulsed speckles experiences similar temporal broadening, as displayed in Fig. 3(H) ($\tau_{570} = 2.1 \pm 0.4$ ps, $\tau_{600} = 2.6 \pm 0.5$ ps, $\tau_{633} = 2.7 \pm 0.1$ ps). This confirms that the system performance, in the considered wavelength range, is wavelength resilient upon calibration. Average beam waist and pulse duration obtained at different λ_i are summarized in Table 1.

Table 1. summary of the different foci parameters obtained at different operational wavelengths

Wavelength	Beam waist (± std)	Pulse duration (± std)
570 nm	4.2 ± 0.9 μm	2.1 ± 0.4 ps
600 nm	4.3 ± 1.1 μm	2.6 ± 0.5 ps
633 nm	4.6 ± 1.1 μm	2.7 ± 0.1 ps

Although switching between different λ_i requires different calibrations, small $\Delta\lambda$ variations around the central wavelengths enable volumetric scanning by leveraging the chromato-axial memory effect, where the product $\lambda \cdot z$ (wavelength and axial plane) is conserved [35,41]. To validate this principle for the case of a scanning beam generated through a pulsed internal reference, a calibration at λ = 600 nm was performed and a shift of $\Delta\lambda$ applied afterwards. For $\lambda + \Delta\lambda = 603$ nm, a shift of the focusing plane of $\Delta z = -135\mu m$ was observed, as shown in Fig. 4(A). The same procedure can be applied for obtaining a positive Δz: for λ - $\Delta\lambda$ = 597 nm, the focusing plane moves by $\Delta z = +137\mu m$. This result is consistent with previous findings [41], and it suggests that the system can be employed to perform volumetric scanning (Fig. 4(B)). Since the depth of focus was measured to be ~ 21 μm (as the FWHM in Fig. 4(C)), the following characterization of the scanning volume was carried at steps of Δz = 22.5 μm (which corresponds to $\Delta\lambda$ = 0.5 nm), to assure not overlapped scanning planes (only the case Δz>0 was considered, more relevant for imaging applications). Figure 4(B) displays the focusing efficiency maps over several scanning planes from Δz = 0 to Δz =112.5 μm, with related histograms in Fig. 4(D). The red circle outlines the effective scanning field (ESF) showing higher and more uniform

Optics EXPRESS

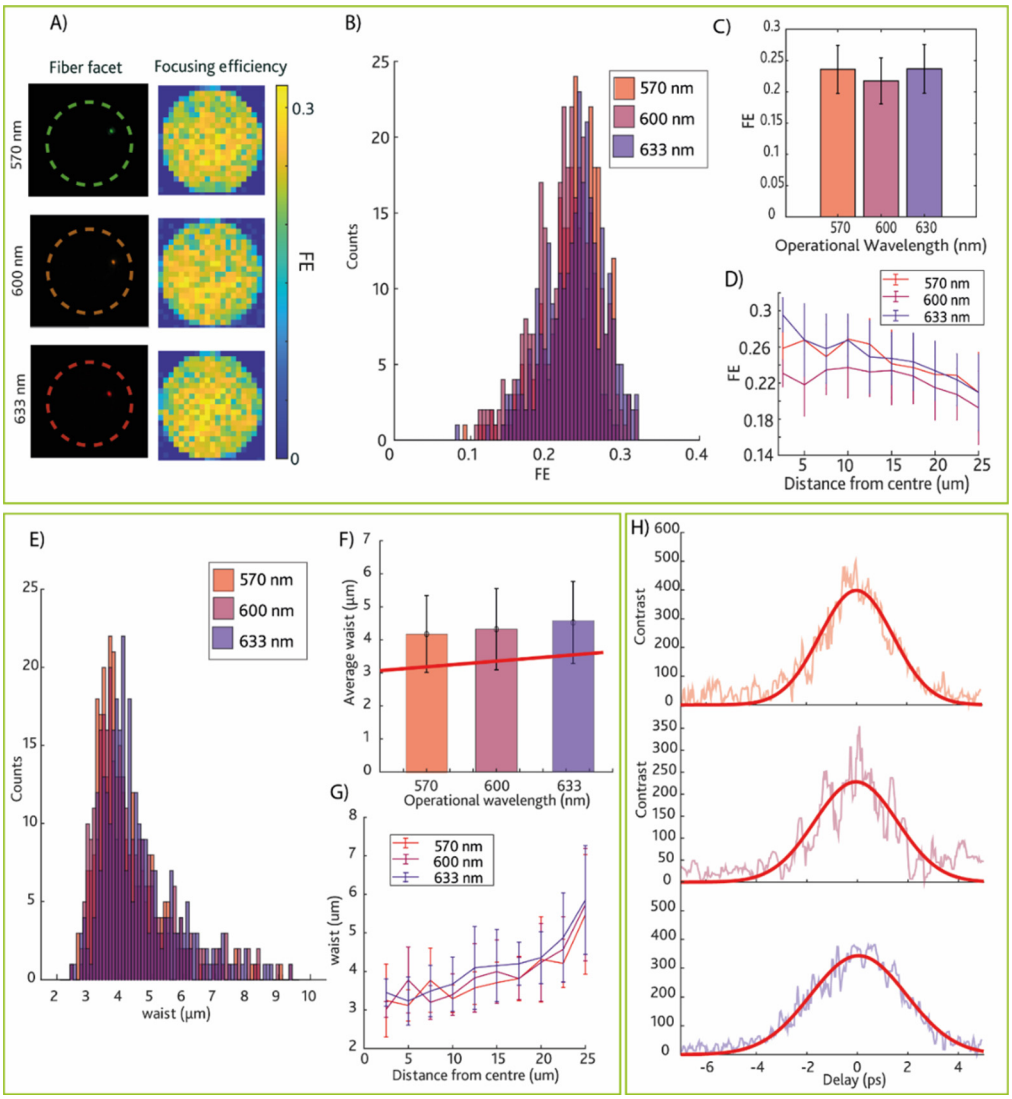

Fig. 3. A) Foci obtained on the distal facet of the fiber for three operational wavelengths and corresponding focusing efficiency intensity maps. B) Focusing efficiency distribution. C) Average focusing efficiency for the three wavelengths. D) Trend of the focusing efficiency in dependence on the distance from the center of the fiber. E) Waist distributions for λ_i F) Average waist for the three operational wavelengths. In Red the corresponding diffraction limit for the MMF calculated for λ_i. G) Trend of waist size in dependence on the distance from the center of the fiber. H) Example of temporal measure performed after MMF with Michelson interferometer: in top panel $\lambda_i = 570\ nm$, central panel $\lambda_i = 600\ nm$, bottom panel $\lambda_i = 633\ nm$.

FE, and outside which distortions of the foci where observed (Visualization 2). Figure 4(E) displays the radius of the identified ESF and its average FE as a function of the distance from the fiber facet Δz. Considering the reduction of the FE as a function of depth, $\Delta z = 90\ \mu m$ represents an upper limit. Within these limits, the volume available for the scan is a truncated cone of $V = 8.77\ 10^4\ \mu m^3$. In the volume considered, the average waist size of the focused spot

Optics EXPRESS

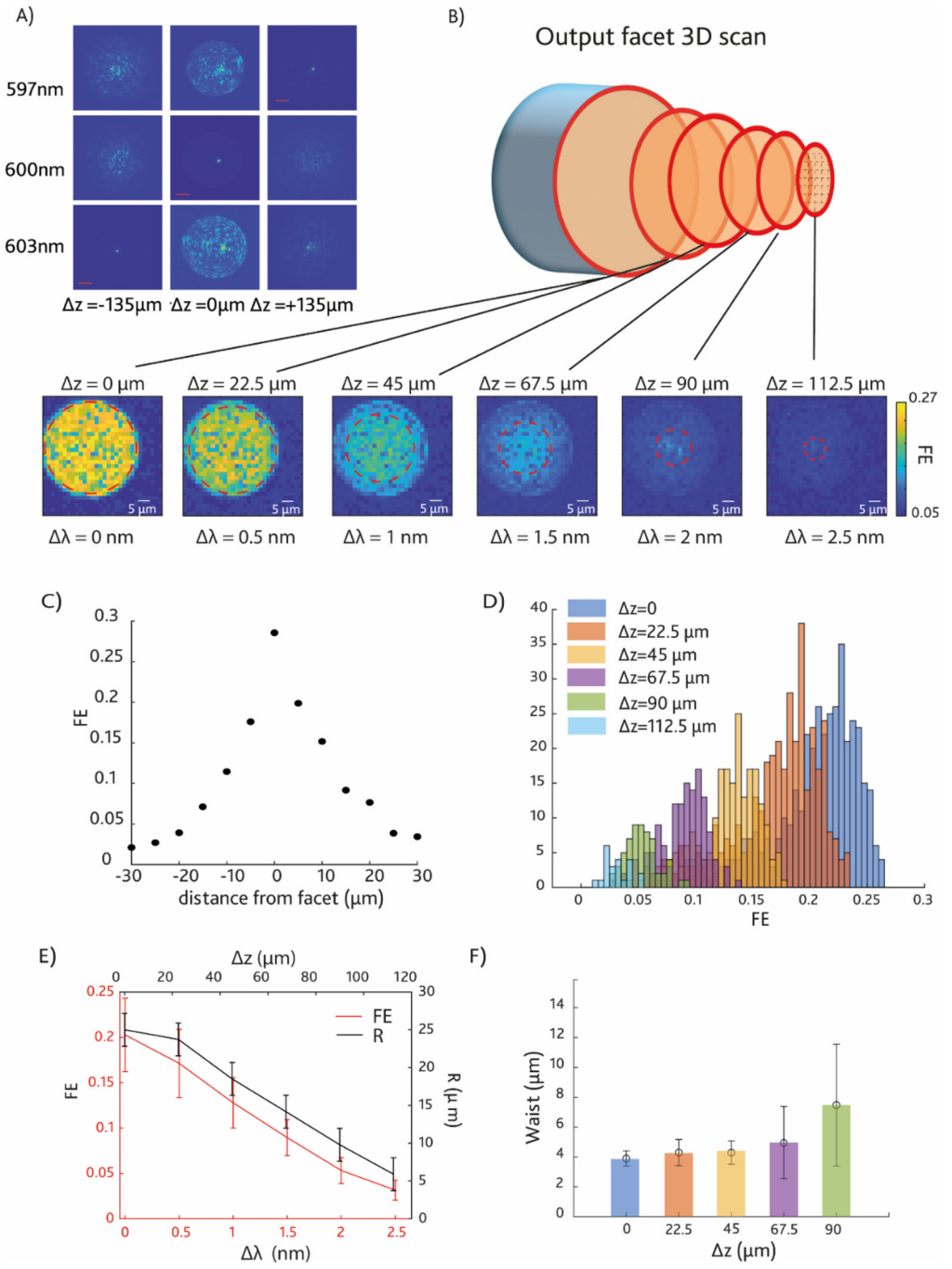

Fig. 4. A) Focusing spot at different z and λ. A shift of ±3 nm corresponds to a $\Delta z = \pm 135\ \mu m$. The scale bar indicates 12 μm. B) Schematic representation of the scanning volume. For each plane the corresponding FE map is presented. The red circle indicates the area not affected by aberration. The scale bar indicates 5 μm. C) FE dependence on the depth for a fixed focused spot on the fiber facet. The wavelength was set to 600 nm. D) FE distribution at different depths from the fiber facet in the available scanning area. E) Radius of the available scanning area (in black) and average FE in the scanning area (in red) as a function of the scanning depth. F) Average waist of the focused spot at different depths from the fiber facet.

Optics EXPRESS

is modified as shown in Fig. 4(F): as the scanning plane moves further from the fiber facet, the waists increase, this is consistent with the angular divergence of the external output modes and with the reduced FE.

3. Discussion and conclusions

We have presented a system for multiplane and multicolor scanning of a supercontinuum source through a MMF, exploiting the advantages of an internal reference beam. The presented data show how this grants a higher focusing efficiency compared to a delayed external reference, with an improvement of 56.4%. This was obtained while keeping a beam waist close very close to the diffraction limit. In addition, the internal reference approach streamlines the optical setup, which do not require external delay lines. Together with these advantages, the internal reference-based technique comes with two relevant drawbacks: the presence of blind spots due to singularities that prevent a uniform focus on the output facet and the loss of information regarding the phase that gets scrambled along the fiber. While the first problem has been recently solved by implementing a multi-reference calibration [36,42], the second concern still stands but does not impact the possibility to apply the internal reference system in traditional imaging applications.

Since both the reference and the probe beams experience a similar optical path within the MMF, a temporal broadening with respect to the original pulse is observed (before the fiber $\tau_{ref} \sim 1.67 \pm 0.10$ ps, after the fiber $\tau_{probe} \sim 2.6 \pm 0.5$ ps). This has to be taken into account when targeting imaging applications requiring pulsed excitation, including FLIM, two-photon microscopy or CARS. In the case of external reference, the delay line acts as a filter selecting only the modes that share similar propagation velocities preserving the duration of the pulse [33]. If, however, the optimization algorithm is based on the use of an internal reference, most of the modes contribute to the interference since both the reference and the probing mode are decomposed in the internal modes of the fiber and undergo similar dispersion phenomena. While this could limit the use of this system in applications that require extreme temporal control, this is compensated by a much higher focusing efficiency, which is beneficial for applications requiring additional power confined inside the focused spot.

In this work we focused on the broadening of the pulse originating by the modal dispersion of the fiber, while we considered negligible the temporal broadening due to the group velocity dispersion(GVD). This assumption was made considering that the maximum temporal broadening due to GVD is given by the formula [43]:

$$\sigma_{max} \approx D_\lambda \Delta\lambda L$$

where D_λ is the dispersion parameter typical of the material, $\Delta\lambda$ is the bandwidth and L is the length of the fiber. In our system the pulse before the MMF was measured to be 1.67 ± 0.1 ps with a corresponding bandwidth of $\sim$1 nm, while the fiber length is 5 cm. At 600 nm $D_\lambda = -292.63 \frac{ps}{km \cdot nm}$, [44] leading to a $\sigma_{max} \approx -0.014\ ps$. If shorter pulses (with a wider bandwidth) or a longer fiber are used, the GVD can be precompensated on the external reference path with the use of a prism pair [28].

In addition to the temporal behavior characterization, the performances of the internal reference approach are resilient on the choice of the operational wavelength in the calibration process, thereby ensuring a good quality focused spot, in a uniform fashion on the entire core of the fiber, and with a diffraction limited waist for all λ_i. This represents an interesting added benefit for imaging applications where different dyes that operate at different excitation wavelengths are required. Lastly, the chromato-axial memory effect [41] can be employed for moving the scanning plane beyond the fiber facet.

Funding. H2020 Marie Skłodowska-Curie Actions (101106602); Robotics and AI for Socio-economic Empowerment (ECS00000035); H2020 LEIT Information and Communication Technologies (101016787); H2020 Future and Emerging Technologies (828972); European Research Council (677683, 692943).

Optics EXPRESS

Acknowledgments. L.C, M.D.V., and Fe.P. acknowledge funding from the European Union's Horizon 2020 Research and Innovation Program under Grant Agreement No. 828972. L.C., M.D.V. and Fe.P. acknowledge funding from the Project "RAISE (Robotics and AI for Socio-economic Empowerment)" code ECS00000035 funded by European Union – NextGenerationEU PNRR MUR - M4C2 – Investimento 1.5 - Avviso "Ecosistemi dell'Innovazione" CUP J33C22001220001. Fi.P., and Fe.P. acknowledge funding from the European Research Council under the European Union's Horizon 2020 Research and Innovation Program under Grant Agreement No. 677683. Fi.P., M.D.V., and Fe.P. acknowledge funding from the European Union's Horizon 2020 Research and Innovation Program under Grant Agreement No 101016787. M.D.V. acknowledges funding from the European Research Council under the European Union's Horizon 2020 Research and Innovation Program under Grant Agreement No. 692943. M.D.V. acknowledges funding from the U.S. National Institutes of Health (Grant No. U01NS094190). M.D.V., and Fe.P. acknowledge funding from the U.S. National Institutes of Health (Grant No. 1UF1NS108177-01). M.D.V and Fe.P acknowledge funding from European Research Council under the European Union's Horizon 2020 Research and Innovation Program under Grant Agreement No. 966674. A.B. acknowledges funding from the European Union's Horizon 2020 research and innovation program under the Marie Sklodowska-Curie grant agreement (#101106602).

Disclosures. M.D.V. and Fe.P. are founders and hold private equity in Optogenix, a company that develops, produces, and sells technologies to deliver light into the brain.

Data availability. The data that support the findings of this study are available from the corresponding author upon reasonable request.

Supplemental document. See Supplement 1 for supporting content.

References

1. S. Turtaev, I. T. Leite, T. Altwegg-Boussac, *et al.*, "High-fidelity multimode fibre-based endoscopy for deep brain in vivo imaging," Light: Sci. Appl. **7**(1), 92 (2018).
2. Y. Hayashi, Y. Tagawa, S. Yawata, *et al.*, "Spatio-temporal control of neural activity *in vivo* using fluorescence microendoscopy," European Journal of Neuroscience **36**(6), 2722–2732 (2012).
3. S. A. Vasquez-Lopez, R. Turcotte, V. Koren, *et al.*, "Subcellular spatial resolution achieved for deep-brain imaging in vivo using a minimally invasive multimode fiber," Light: Sci. Appl. **7**(1), 110 (2018).
4. C. Zeng, Z. Chen, H. Yang, *et al.*, "Advanced high resolution three-dimensional imaging to visualize the cerebral neurovascular network in stroke," Int. J. Biol. Sci. **18**(2), 552–571 (2022).
5. U. Weiss and O. Katz, "Two-photon lensless micro-endoscopy with in-situ wavefront correction," Opt. Express **26**(22), 28808 (2018).
6. N. Accanto, F. G. C. Blot, A. Lorca-Cámara, *et al.*, "A flexible two-photon fiberscope for fast activity imaging and precise optogenetic photostimulation of neurons in freely moving mice," Neuron **111**(2), 176–189.e6 (2023).
7. W. Choi, M. Kang, J. H. Hong, *et al.*, "Flexible-type ultrathin holographic endoscope for microscopic imaging of unstained biological tissues," Nat. Commun. **13**(1), 4469 (2022).
8. A. Sattin, A. Antonini, S. Bovetti, *et al.*, "Extended field-of-view microendoscopy through aberration corrected GRIN lenses," *Advances in Microscopic Imaging II,* E. Pavone, P. T. Beaurepaire, and So, eds., 54, SPIE (2019).
9. H. Cao, T. Čižmár, S. Turtaev, *et al.*, "Controlling light propagation in multimode fibers for imaging, spectroscopy and beyond," Adv. Opt. Photon. **15**(2), 524 (2023).
10. R. Di Leonardo and S. Bianchi, "Hologram transmission through multi-mode optical fibers," Opt. Express **19**(1), 247 (2011).
11. G. X. Wu, R. Z. Zhu, Y. Q. Lu, *et al.*, "Optical scanning endoscope via a single multimode optical fiber," Opto-Electron. Sci. **3**(3), 230041 (2024).
12. T. Čižmár and K. Dholakia, "Shaping the light transmission through a multimode optical fibre: complex transformation analysis and applications in biophotonics," Opt. Express **19**(20), 18871 (2011).
13. L. Collard, F. Pisano, D. Zheng, *et al.*, "Holographic Manipulation of Nanostructured Fiber Optics Enables Spatially-Resolved, Reconfigurable Optical Control of Plasmonic Local Field Enhancement and SERS," Small **18**(23), 2200975 (2022).
14. I. N. Papadopoulos, S. Farahi, C. Moser, *et al.*, "Focusing and scanning light through a multimode optical fiber using digital phase conjugation," Opt. Express **20**(10), 10583 (2012).
15. L. Collard, F. Pisano, M. Pisanello, *et al.*, "Wavefront engineering for controlled structuring of far-field intensity and phase patterns from multimodal optical fibers," APL Photonics **6**(5), 051301 (2021).
16. I. N. Papadopoulos, S. Farahi, C. Moser, *et al.*, "High-resolution, lensless endoscope based on digital scanning through a multimode optical fiber," Biomed. Opt. Express **4**(2), 260 (2013).
17. M. N'Gom, T. B. Norris, E. Michielssen, *et al.*, "Mode control in a multimode fiber through acquiring its transmission matrix from a reference-less optical system," Opt. Lett. **43**(3), 419 (2018).
18. C. Shengfu, Z. Xuyu, and Z. Tianting, "Nonconvex optimization for optimum retrieval of the transmission matrix of a multimode fiber," Adv. Photon. Nexus **2**(6), 066005 (2023).
19. W. Li, K. Abrashitova, G. Osnabrugge, *et al.*, "Generative Adversarial Network for Superresolution Imaging through a Fiber," Phys. Rev. Applied **18**(3), 034075 (2022).
20. B. Rahmani, I. Oguz, U. Tegin, *et al.*, "Learning to image and compute with multimode optical fibers," Nanophotonics **11**(6), 1071–1082 (2022).

Optics EXPRESS

21. L. Collard, M. Kazemzadeh, Piscopo, *et al.*, "Exploiting holographically end variance to transmit labelled images through a multimode optical fiber," Opt. Express **32**(11), 18896 (2024).
22. S. Resisi, S. M. Popoff, and Y. Bromberg, "Image Transmission Through a Dynamically Perturbed Multimode Fiber by Deep Learning," Laser Photon Rev **15**(10), 2000553 (2021).
23. S. Goel, C. Conti, S. Leedumrongwatthanakun, *et al.*, "Referenceless characterization of complex media using physics-informed neural networks," Opt. Express **31**(20), 32824 (2023).
24. A. D. Gomes, S. Turtaev, Y. Du, *et al.*, "Near perfect focusing through multimode fibres," Opt. Express **30**(7), 10645 (2022).
25. M. Stibůrek, P. Ondráčková, T. Tučková, *et al.*, "110 µm thin endo-microscope for deep-brain in vivo observations of neuronal connectivity, activity and blood flow dynamics," Nat Commun **14**(1), 1897 (2023).
26. W. Li, K. Abrashitova, and L. V. Amitonova, "Super-resolution multimode fiber imaging with an untrained neural network," Opt. Lett. **48**(13), 3363 (2023).
27. D. Stellinga, D. B. Phillips, S. P. Mekhail, *et al.*, "Time-of-flight 3D imaging through multimode optical fibers," Science (1979) **374**(6573), 1395–1399 (2021).
28. E. E. Morales-Delgado, D. Psaltis, and C. Moser, "Two-photon imaging through a multimode fiber," Opt. Express **23**(25), 32158 (2015).
29. S. Sivankutty, E. R. Andresen, R. Cossart, *et al.*, "Ultra-thin rigid endoscope: two-photon imaging through a graded-index multi-mode fiber," Opt. Express **24**(2), 825–841 (2016).
30. E. Pedretti, M. G. Tanner, T. R. Choudhary, *et al.*, "High-speed dual color fluorescence lifetime endomicroscopy for highly-multiplexed pulmonary diagnostic applications and detection of labeled bacteria," Biomed Opt Express **10**(1), 181 (2019).
31. J. Trägårdh, T. Pikálek, M. Šerý, *et al.*, "Label-free CARS microscopy through a multimode fiber endoscope," Opt. Express **27**(21), 30055 (2019).
32. A. Cifuentes, T. Pikálek, P. Ondráčková, *et al.*, "Polarization-resolved second-harmonic generation imaging through a multimode fiber," Optica **8**(8), 1065 (2021).
33. E. E. Morales-Delgado, S. Farahi, I. N. Papadopoulos, *et al.*, "Delivery of focused short pulses through a multimode fiber," Opt. Express **23**(7), 9109 (2015).
34. M. C. Velsink, L. V. Amitonova, and P. W. H. Pinkse, "Spatiotemporal focusing through a multimode fiber via time-domain wavefront shaping," Opt. Express **29**(1), 272 (2021).
35. T. Čižmár and K. Dholakia, "Exploiting multimode waveguides for pure fibre-based imaging," Nat Commun **3**(1), 1027 (2012).
36. L. Collard, L. Piscopo, F. Pisano, *et al.*, "Optimizing the internal phase reference to shape the output of a multimode optical fiber," PLoS One **18**(9), e0290300 (2023).
37. T. Pikálek, J. Trägårdh, S. Simpson, *et al.*, "Wavelength dependent characterization of a multimode fibre endoscope," Opt. Express **27**(20), 28239 (2019).
38. R. R. Alfano, ed., *[The Supercontinuum Laser Source, Second Edition]*, Springer-Verlag, New York (2006).
39. C. C. Schmidt, R. Turcotte, M. J. Booth, *et al.*, "Repeated imaging through a multimode optical fiber using adaptive optics," Biomed Opt Express **13**(2), 662 (2022).
40. A. Descloux, L. V. Amitonova, and P. W. H. Pinkse, "Aberrations of the point spread function of a multimode fiber due to partial mode excitation," Opt. Express **24**(16), 18501 (2016).
41. L. Devaud, M. Guillon, I. Gusachenko, *et al.*, "Chromato-axial memory effect in step-index multimode fibers," APL Photonics **6**(12), 126105 (2021).
42. P. Jákl, M. Šiler, J. Ježek, *et al.*, "Endoscopic Imaging Using a Multimode Optical Fibre Calibrated with Multiple Internal References," Photonics **9**(1), 37 (2022).
43. E. E. Morales Delgado, "Control of pulsed light propagation through multimode optical fibers," Lausanne, EPFL 122, (2017).
44. J. Diels and W. Rudolf, *Ultrashort Laser Pulse Phenomena*, Second Edition (Massachusetts, Academic Press, 2006).